

May 2020

ALFALFA Harvest: HI Imaging and 3D Modeling of Candidate Local Group Dwarf Galaxies

Lilly Bralts-Kelly
Macalester College, lbraltsk@macalester.edu

Susie Paine
Macalester College, spaine@macalester.edu

Elizabeth A. K. Adams
ASTRON, adams@astron.nl

John M. Cannon
Macalester College, jcannon@macalester.edu

Follow this and additional works at: <https://digitalcommons.macalester.edu/mjpa>



Part of the [Astrophysics and Astronomy Commons](#), and the [Physics Commons](#)

Recommended Citation

Bralts-Kelly, Lilly; Paine, Susie; Adams, Elizabeth A. K.; and Cannon, John M. (2020) "ALFALFA Harvest: HI Imaging and 3D Modeling of Candidate Local Group Dwarf Galaxies," *Macalester Journal of Physics and Astronomy*. Vol. 8: Iss. 1, Article 2.

Available at: <https://digitalcommons.macalester.edu/mjpa/vol8/iss1/2>

This Capstone is brought to you for free and open access by the Physics and Astronomy Department at DigitalCommons@Macalester College. It has been accepted for inclusion in Macalester Journal of Physics and Astronomy by an authorized editor of DigitalCommons@Macalester College. For more information, please contact scholarpub@macalester.edu.

ALFALFA Harvest: HI Imaging and 3D Modeling of Candidate Local Group Dwarf Galaxies

Abstract

Isolated neutral hydrogen (HI) clouds, or "ultra-compact high-velocity clouds" (UCHVCs), form a small subset of detections by the Arecibo Legacy Fast ALFA (ALFALFA) blind extragalactic survey. These systems, if located within ~ 1 Mpc, would populate the lowest-mass end of the HI mass function. Subsequent optical imaging has revealed that some of these UCHVCs harbor associated (though sparse) stellar populations, suggesting that they may be some of the most extreme galaxies known in the Local Volume, with properties akin to ultra-faint dwarf galaxies but with significant neutral gas reservoirs. In this work, we investigate the neutral hydrogen properties of six UCHVC candidate galaxies using deep spectral line imaging from the Karl G. Jansky Very Large Array (VLA). We produce images and discuss the morphological and kinematic properties of six sources: AGC 198606, AGC 215417, AGC 219656, AGC 249525, AGC 258237, and AGC 268069. We also apply the modeling code 3D-Barolo to our deep HI images in order to derive rotation curves and constrain inclination angles for our two most promising galaxy candidates: AGC 198606 and AGC 249525. Successful modeling allows us to determine the dynamical masses of these objects and thus to consider them in the context of various fundamental scaling relations defined by more massive galaxies.

Keywords

extragalactic astronomy, radio astronomy, dwarf galaxies, neutral hydrogen

ALFALFA Harvest: HI Imaging and 3D Modeling of Candidate Local Group Dwarf Galaxies

Lilly Bralts-Kelly¹, Susannah Paine¹, Elizabeth A. K. Adams², John M. Cannon¹

¹*Macalester College*, ²*ASTRON*

April 2020

Abstract

Isolated neutral hydrogen (HI) clouds, or “ultra-compact high-velocity clouds” (UCHVCs), form a small subset of detections by the Arecibo Legacy Fast ALFA (ALFALFA) blind extragalactic survey. These systems, if located within ~ 1 Mpc, would populate the lowest-mass end of the HI mass function. Subsequent optical imaging has revealed that some of these UCHVCs harbor associated (though sparse) stellar populations, suggesting that they may be some of the most extreme galaxies known in the Local Volume, with properties akin to ultra-faint dwarf galaxies but with significant neutral gas reservoirs. In this work, we investigate the neutral hydrogen properties of six UCHVC candidate galaxies using deep spectral line imaging from the Karl G. Jansky Very Large Array (VLA). We produce images and discuss the morphological and kinematic properties of six sources: AGC 198606, AGC 215417, AGC 219656, AGC 249525, AGC 258237, and AGC 268069. We also apply the modeling code 3D-Barolo to our deep HI images in order to derive rotation curves and constrain inclination angles for our two most promising galaxy candidates: AGC 198606 and AGC 249525. Successful modeling allows us to determine the dynamical masses of these objects and thus to consider them in the context of various fundamental scaling relations defined by more massive galaxies.

1 Introduction

According to the current Λ CDM cosmological model and associated numerical simulations, the universe should be teeming with relatively low mass halos registering masses $\lesssim 10^9 M_\odot$ (Bullock & Boylan-Kolchin, 2017). However, observations show an absence of such halos that is most obvious in the Local Group, where the number of dwarf satellites and nearby galaxies is significantly smaller than expected by models of the Milky Way. This discrepancy is often referred to as the “missing satellites problem” (Klypin et al., 1999) or, alternately, the “void problem” (Peebles, 2001), and is generally attributed to the effects of star formation feedback and reionization, which result in dark matter halos not hosting observable galaxies. We seek to better understand the specifics of these effects as they relate to low-mass galaxy evolution. To do so, we require a population of low-mass galaxies near enough to be detected, but distant enough to avoid modification of their intrinsic properties from interaction with the Milky Way. Such objects have proved elusive. In order to be detected in large optical surveys like the Sloan Digital Sky Survey (SDSS), they must be close enough to the Milky Way to have largely lost their gas component; but if they are distant enough to have avoided such interactions, their stellar components fall below the detection limit for the same optical surveys.

Therefore, in order to locate a population that meets these conditions, we must search outside of the visible spectrum. The neutral hydrogen spectral line is an excellent candidate for such a search, as it allows us to identify isolated galaxies that may be gas-rich but optically faint; Leo P and Leo T are examples of such sources (McQuinn et al., 2015; Adams & Oosterloo, 2018). Leo P is an example of a source originally identified as The Arecibo Legacy Fast ALFA (ALFALFA) blind extragalactic survey has the capability to detect sources termed “ultra-compact high-velocity clouds” (UCHVCs), or isolated HI clouds, classified according to criteria detailed in Adams et al. (2013). Briefly, these criteria limit the ALFALFA catalog to strong detections with sizes and velocities consistent with Local Volume galaxies. They also emphasize isolation from known HVC complexes in order to distinguish sources that may be extragalactic from those that are more likely local. Lastly, it is required that these sources have no optical counterpart found in SDSS or DSS; if such

a counterpart existed, these sources would already be identified as galaxies.

Of the ~ 30000 sources detected and cataloged in the ALFALFA database, approximately 100 have been identified as UCHVCs. These sources were first posited as being candidate low-mass galaxies by [Giovanelli et al. \(2010\)](#); since then, [Adams et al. \(2013\)](#) presented work on a subset of the UCHVC population for the 40% complete ALFALFA survey, and later [Adams et al. \(2016\)](#) followed up on several of these sources with HI imaging using the Westerbork Synthesis Radio Telescope; at high enough resolution, these observations could aid in distinguishing between likely galactic halo clouds and external galaxy candidates. This study originally identified the six sources presented here as promising galaxy candidates within the UCHVC population.

[Adams et al. \(2013\)](#) and [Adams et al. \(2016\)](#) also provided the foundation for a search for UCHVC stellar counterparts using the WIYN 3.5m telescope. [Janesh et al. \(2015\)](#) found a possible optical counterpart to the ALFALFA source AGC 198606, and [Janesh et al. \(2017\)](#) yielded a similar results for AGC 249525. [Janesh et al. \(2019\)](#) again surveyed these sources, among others, and found stellar overdensities that are likely associated with five UCHVCs. For these systems, originally identified as good galaxy candidates based on HI imaging, the presence of stars is more compelling evidence for their candidacy. We choose these five, as well as a sixth marginal detection from [Janesh et al. \(2019\)](#), for follow-up observations with the Karl G. Jansky Very Large Array (VLA). Using our deep HI images, we apply the modeling software 3D-Barolo to derive rotation curves for a subset of these objects, a crucial first step leading to future work on their dark matter content.

2 Observations

These six sources were observed between 2015 and 2018 using the Karl G. Jansky VLA in the D configuration, under programs 15B-079 and 18A-198.

All data were reduced in the Common Astronomy Software Applications package (CASA, [McMullin et al., 2007](#)). The data were flagged manually for radio frequency interference (RFI) and cross calibration was performed following standard procedures. A

Name (1)	RA+Dec J2000 (2)	cz km s^{-1} (3)	W_{50} km s^{-1} (4)	S_{HI} Jy km s^{-1} (5)	$\log \bar{N}_{\text{HI}}$ atoms cm^{-2} (6)
AGC 198606	09h30 ^m 05 ^s .5+16 ^d 39 ^m 03 ^s	53	21	6.73 ± 0.67	19.6
AGC 215417	11h40 ^m 08 ^s .1+15 ^d 06 ^m 44 ^s	216	17	0.70 ± 0.07	18.5
AGC 219656	11h51 ^m 24 ^s .3+20 ^d 32 ^m 20 ^s	192	21	0.85 ± 0.08	18.8
AGC 249525	14h17 ^m 50 ^s .1+17 ^d 32 ^m 52 ^s	48	24	6.73 ± 0.67	19.6
AGC 258237	15h07 ^m 23 ^s .0+11 ^d 32 ^m 56 ^s	155	23	1.34 ± 0.13	19.1
AGC 268069	16h05 ^m 32 ^s .6+14 ^d 59 ^m 20 ^s	132	29	1.14 ± 0.11	19.0

Table 1: ALFALFA HI properties of our six sources. Columns are as follows: (1) identification number in the Arecibo General Catalog (AGC); (2) equatorial J2000 coordinates of the HI centroid; (3) recessional velocity in the heliocentric frame; (4) HI line full width at half maximum; (5) integrated flux density; (6) the base-10 logarithm of the average column density based on source size and flux, \bar{N}_{HI} .

first-order fit to line-free channels was used to perform continuum emission subtraction in the uv -plane. Imaging of the reduced data was conducted using the CASA task CLEAN, at a consistent spectral resolution of 2.5 km/s for all sources.

A dirty cube was produced in order to identify which channels contained emission from the source. Source emission was selected for cleaning using clean masks, ensuring that all flux is recovered and that noise properties remain unchanged during the cleaning process. Given the particularly low surface brightness and signal-to-noise ratio (SNR) of these objects, a special clean mask was created for each source and used for all channels believed to contain real emission. Each clean mask was produced by collapsing the data along the spectral axis into a single channel, centered at the ALFALFA central velocity and encompassing the full velocity extent of the emission, extending beyond the ALFALFA W_{50} value. This single-channel image was cleaned using a Gaussian taper in the uv -plane to bring it as close as possible to a circular beam of $105''$, and clipped at the 2σ value in order to isolate higher-SNR emission. Manual selection of emission was also performed to eliminate random noise peaks that were not spatially or spectrally co-located with the source. This process was iterated two to four times until a final mask was reached.

Channels to be masked were selected by examining the dirty cube and identifying channels containing emission. The single-channel clean mask was then applied to all those

Name (1)	SCB S_{HI} Jy km s ⁻¹ (2)	SCB $\log \hat{N}_{\text{HI}}$ atoms cm ⁻² (3)	PCB S_{HI} Jy km s ⁻¹ (4)	PCB $\log \hat{N}_{\text{HI}}$ atoms cm ⁻² (5)
AGC 198606	5.98	19.5	6.11	19.5
AGC 215417	0.68	18.8	0.55	18.7
AGC 219656	0.46	18.8	0.51	18.8
AGC 249525	3.69	19.6	3.92	19.6
AGC 258237	1.03	19.2	1.07	19.2
AGC 268069	2.20	19.4	1.98	19.4

Table 2: VLA HI integrated flux density and peak column densities of our six sources. Columns are as follows: (1) identification number in the Arecibo General Catalog (AGC); (2) integrated flux density found using single-channel blanking (SCB); (3) base-10 logarithm of the *peak* column density \hat{N}_{HI} found using SCB; (4) integrated flux density found using per-channel blanking (PCB); (5) the base-10 logarithm of the *peak* column density \hat{N}_{HI} found using PCB.

channels. Each dataset was then cleaned to half the rms value, again tapering close to a circular beam of 105'', for comparison with prior work done by [Adams et al. \(2016\)](#).

In order to find the best probe of the faint neutral gas in these sources, moment maps were created using two different methods. The results of both methods are presented for side-by-side comparison in Figures 1, 2, 3, 4, 5, and 6. In each figure, moment zero maps show total intensity of the HI emission; moment one maps represent the velocity field, and are further blanked to show only the highest-SNR regions from the moment zero map. HI properties of each source were also calculated using both methods for comparison; the results of these calculations are given in Table 2. The methods themselves are briefly explained below.

2.1 Single-channel blanking

Reduced and cleaned data cubes are initially smoothed to a consistent circular beam of 105'', then immediately collapsed into moment zero and one maps over the channel range containing source emission. These moment maps are then blanked at the 2σ level. This method is designed to provide greater sensitivity to low surface brightness emission that may appear in only a few channels.

The left columns of Figures 1, 2, 3, 4, 5, and 6 use single-channel blanking.

2.2 Per-channel blanking

Reduced and cleaned data cubes are initially smoothed to a consistent circular beam of $105''$, then threshold blanked at the 1.5σ level. The resulting cubes are then manually examined for the purpose of isolating emission that is spatially and spectrally contiguous. These cubes are finally collapsed into moment zero and one maps. This method is designed to highlight coherent kinematic structure in the primary cloud while still incorporating the contributions of emission that may appear in only one or a few channels.

The right columns of Figures 1, 2, 3, 4, 5, and 6 use per-channel blanking.

2.3 Comparison of methods

The two methods are not consistent in recovering more or less flux versus the other. Single-channel blanking yields a greater flux integral for sources AGC 215417 and AGC 268069; per-channel blanking yields the greater value for the other four sources. However, if we take the uncertainty on each flux integral to be 10% of the value as in Adams et al. (2016), we do find that the results of the two methods generally agree with each other within those uncertainties. We also note that the peak column densities are largely consistent between methods.

2.4 Comparison to ALFALFA

We note that both methods of blanking yield consistently lower integrated flux densities than the ALFALFA measurements. In the case of AGC 249525, both methods produce a S_{HI} value that is only about 50% of the ALFALFA value. This indicates that the imaging process should be improved in order to verify that we recover all the flux detected by ALFALFA. One possible solution is to perform additional smoothing between the original collapse of channels into a moment map and the subsequent threshold clipping; if the source emission

is at the level of the noise, this may help with flux recovery.

One exception to this phenomenon is AGC 268069; the flux densities found upon examination of the new VLA images nearly double the values previously found with ALFALFA. The peak column density value in the new VLA images is also much larger than the ALFALFA measurement. One explanation for this outlier may be the odd HI morphology of AGC 268069; if the source consists of multiple clouds, then ALFALFA may have identified AGC 268069 as being only one of them, which would naturally produce much lower flux and average column density measurements. This is discussed further in section [4.1](#).

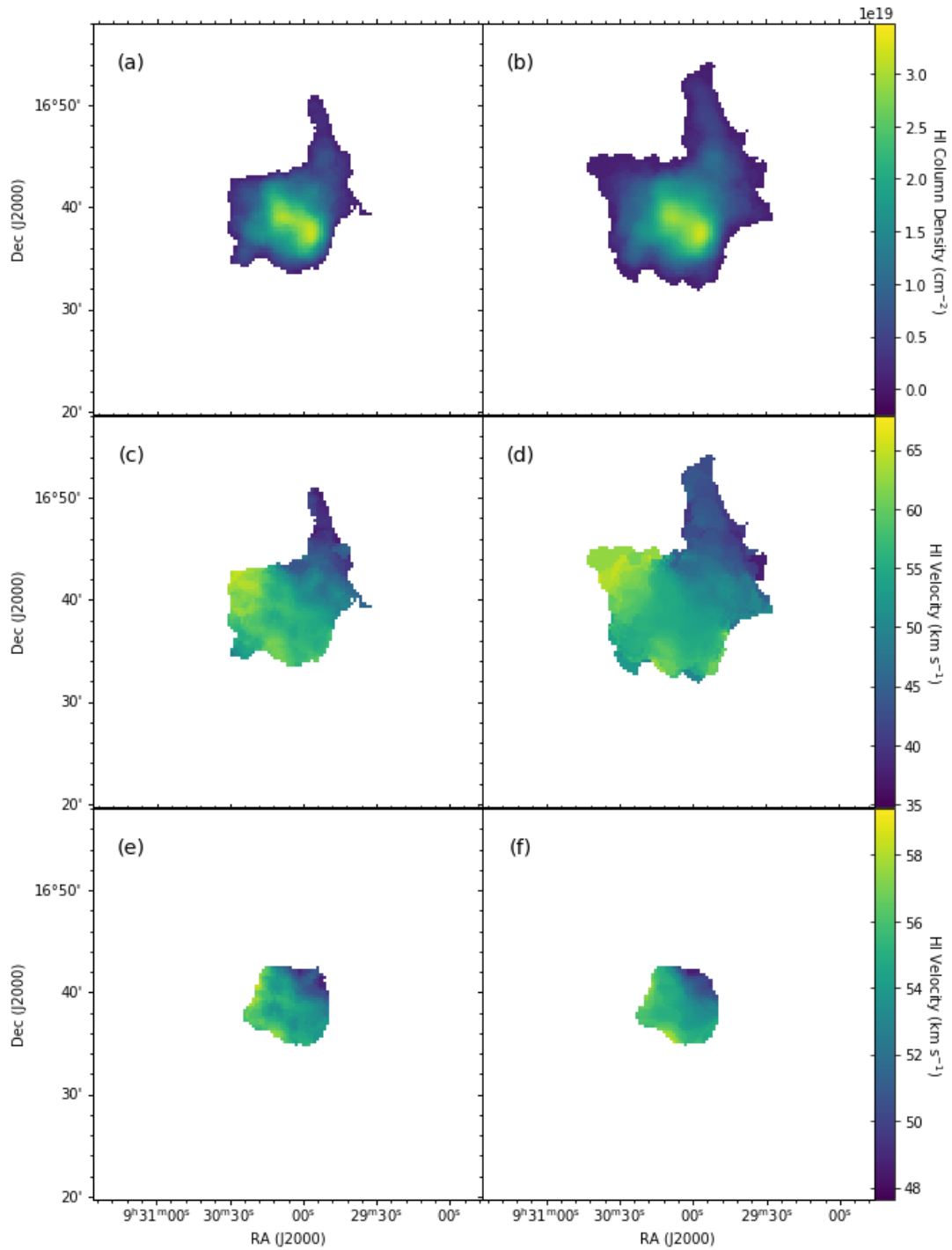


Figure 1: HI images of AGC 198606, applying two methods of moment map creation: single-channel blanking (left column, section 2.1) and per-channel blanking (right column, section 2.2). The moment zero maps in panels (a) and (b) show HI column densities in units of cm^{-2} . The velocity fields shown in panels (c) and (d) are further threshold blanked to highlight a coherent gradient in (e) and (f).

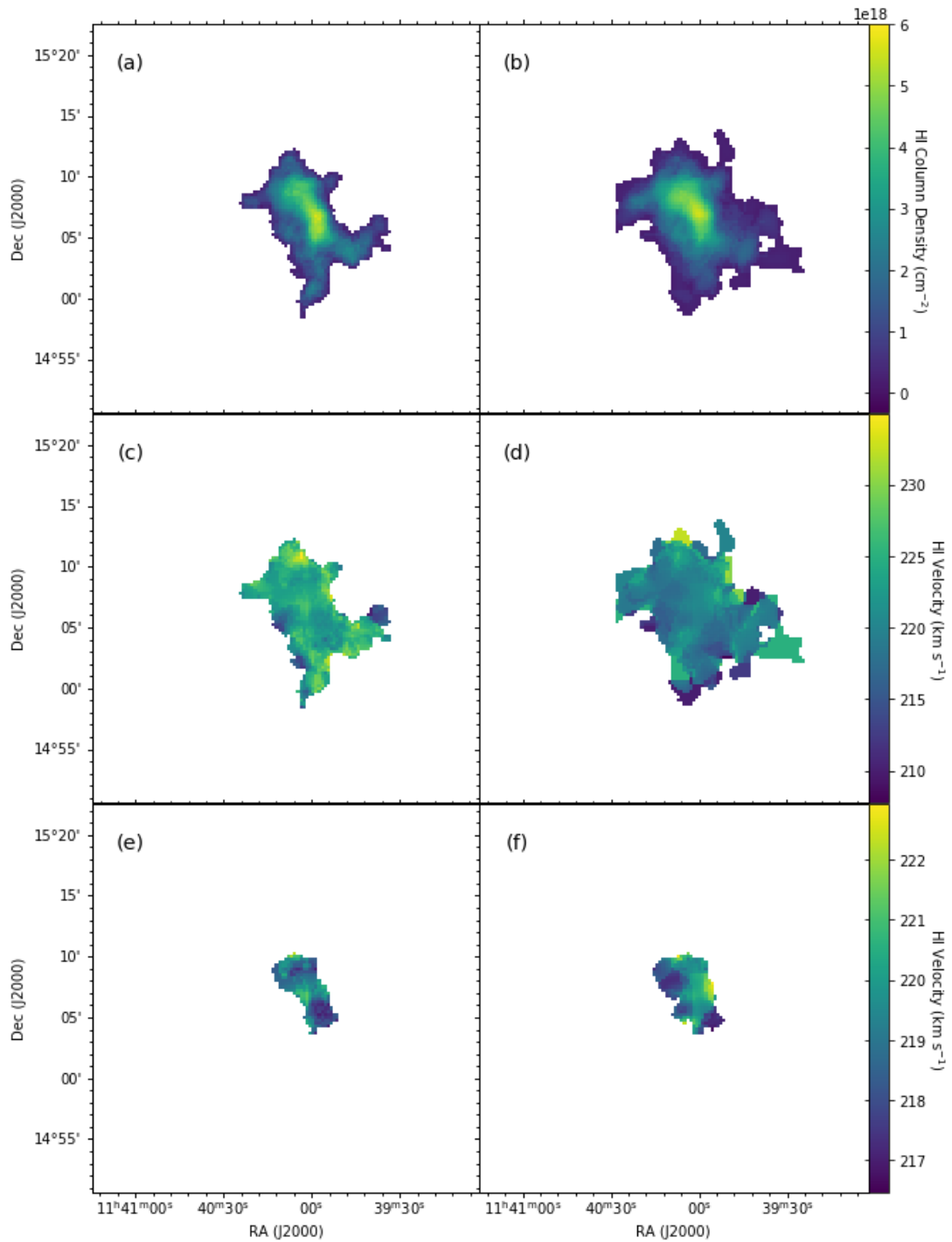


Figure 2: HI images of AGC 215417, applying two methods of moment map creation: single-channel blanking (left column, section 2.1) and per-channel blanking (right column, section 2.2). The moment zero maps in panels (a) and (b) show HI column densities in units of cm^{-2} . The velocity fields shown in panels (c) and (d) are further threshold blanked to highlight a coherent gradient in (e) and (f).

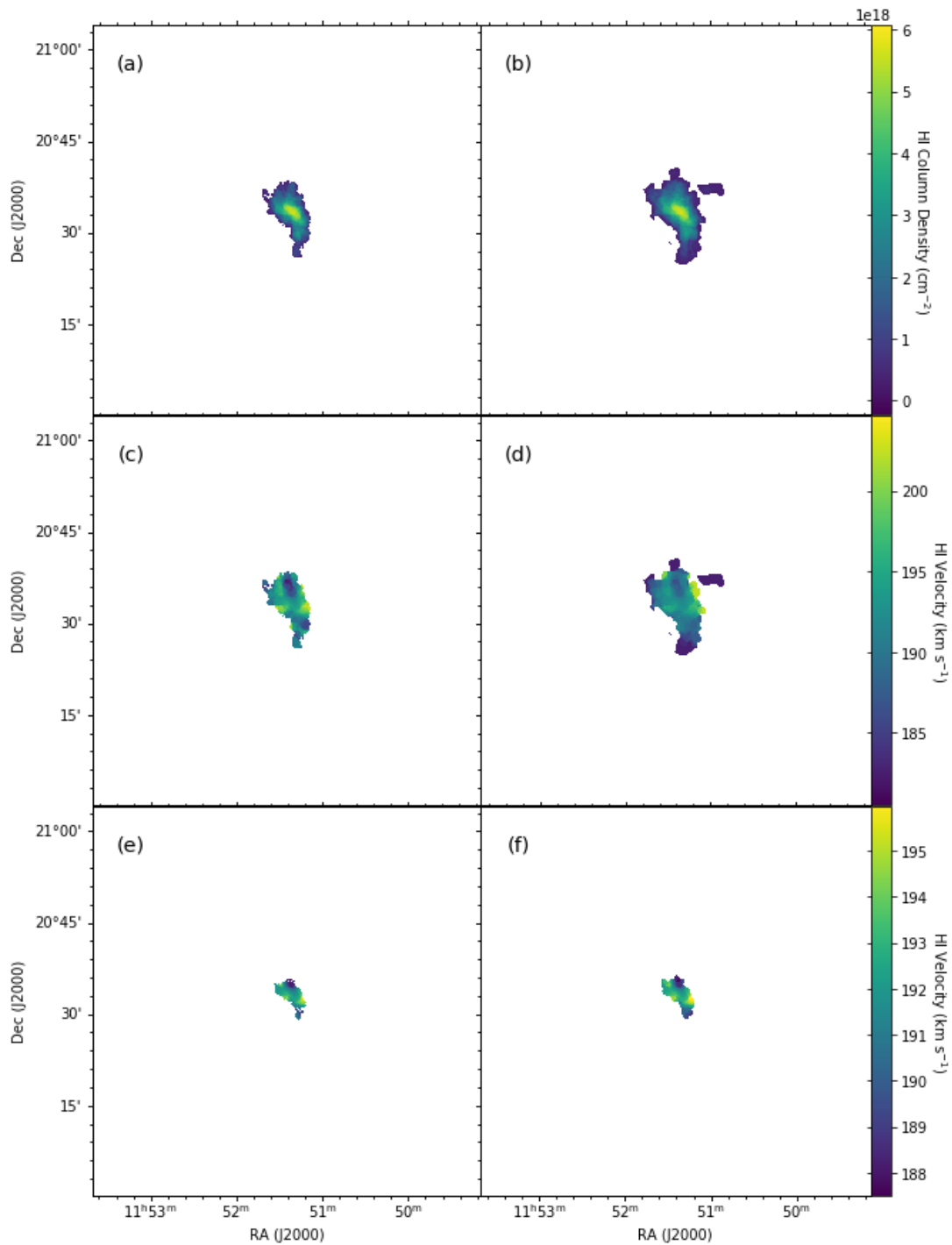


Figure 3: HI images of AGC 219656, applying two methods of moment map creation: single-channel blanking (left column, section 2.1) and per-channel blanking (right column, section 2.2). The moment zero maps in panels (a) and (b) show HI column densities in units of cm^{-2} . The velocity fields shown in panels (c) and (d) are further threshold blanked to highlight a coherent gradient in (e) and (f).

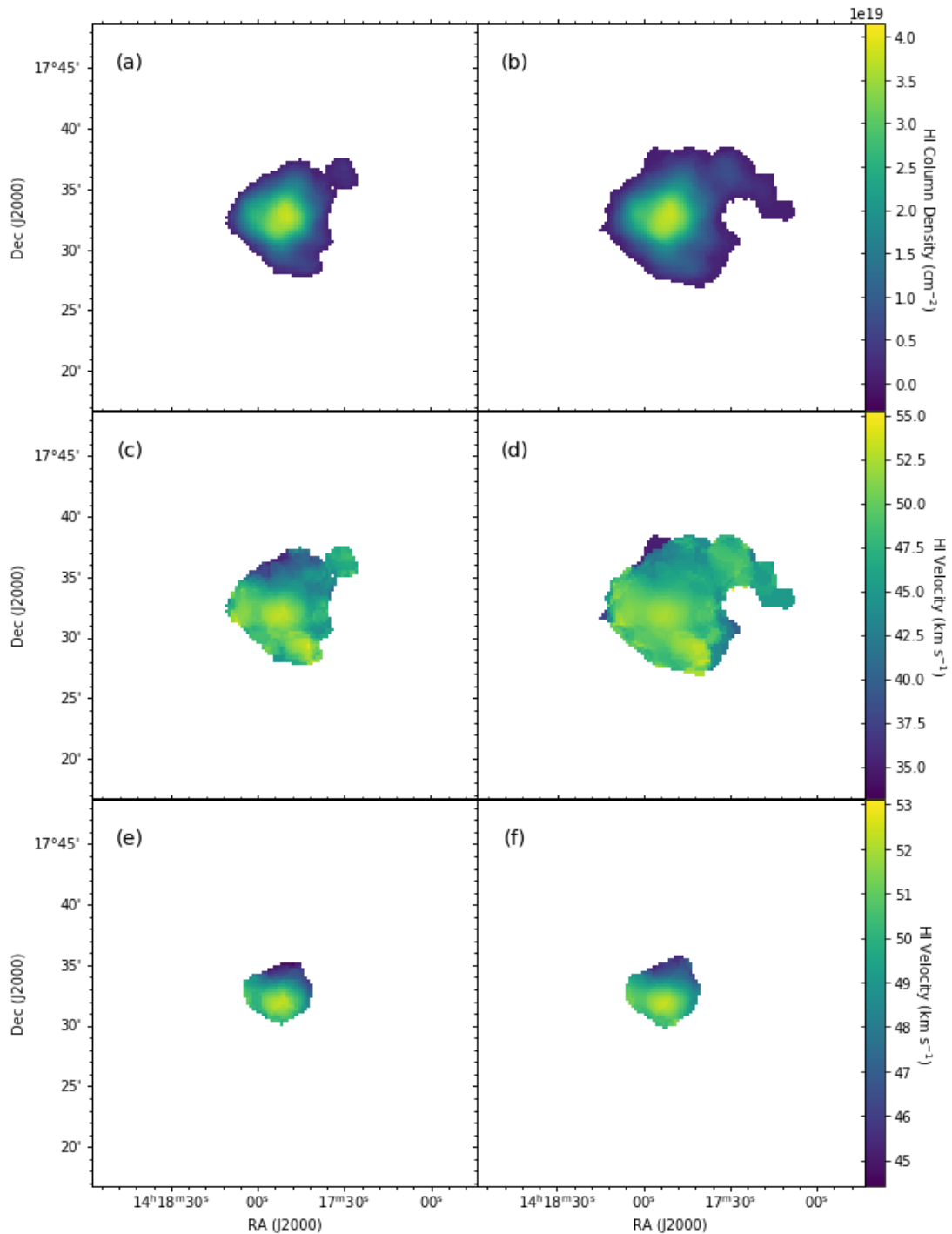


Figure 4: HI images of AGC 249525, applying two methods of moment map creation: single-channel blanking (left column, section 2.1) and per-channel blanking (right column, section 2.2). The moment zero maps in panels (a) and (b) show HI column densities in units of cm^{-2} . The velocity fields shown in panels (c) and (d) are further threshold blanked to highlight a coherent gradient in (e) and (f).

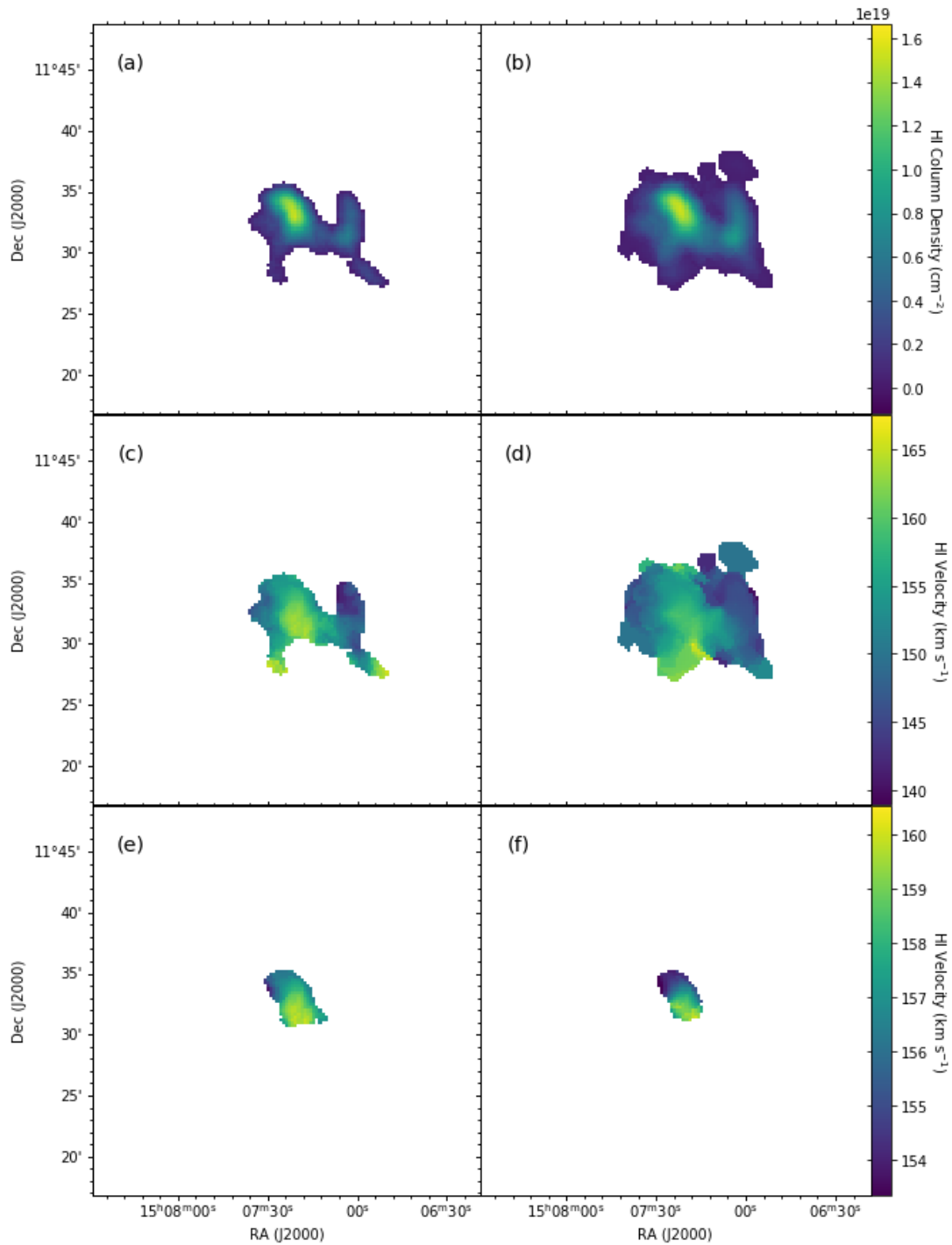


Figure 5: HI images of AGC 258237, applying two methods of moment map creation: single-channel blanking (left column, section 2.1) and per-channel blanking (right column, section 2.2). The moment zero maps in panels (a) and (b) show HI column densities in units of cm^{-2} . The velocity fields shown in panels (c) and (d) are further threshold blanked to highlight a coherent gradient in (e) and (f).

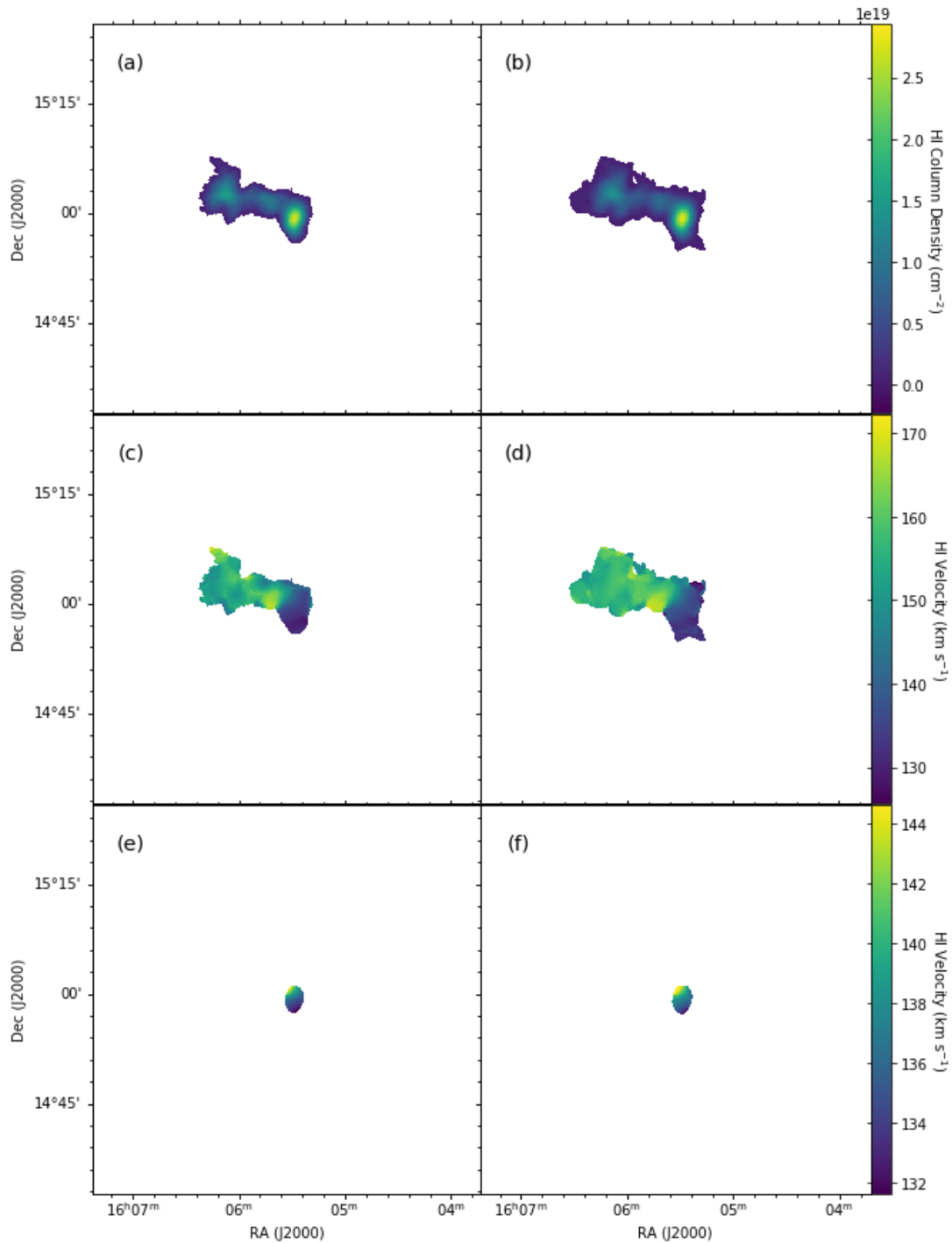


Figure 6: HI images of AGC 268069, applying two methods of moment map creation: single-channel blanking (left column, section 2.1) and per-channel blanking (right column, section 2.2). The moment zero maps in panels (a) and (b) show HI column densities in units of cm^{-2} ; here we note the apparent separation of the HI into multiple distinct clouds. The velocity fields shown in panels (c) and (d) are further threshold blanked to highlight a coherent gradient in (e) and (f).

3 Kinematic modeling

3.1 Procedures

The code 3D-Based Analysis of Rotating Objects from Line Observations (3D-Barolo, [Di Teodoro & Fraternali, 2015](#)) fits 3D tilted-ring models of sources to user-provided spectral line data cubes. Here, we apply this code to several of our cleaned and tapered VLA data cubes, smoothed to a consistent circular beam of $105''$. Instead of threshold blanking by hand, we take advantage of 3D-Barolo's built-in source finder, imposing SNR and spatial and spectral adjacency cuts in order to isolate the primary cloud in each object.

The inclination for each source is constrained by first producing a two-ring base model of the object in order to fix rotational and dispersion velocities, density profiles, and various other parameters. Once these properties have been established, we create many new models, iterating the inclination between 10° and 90° at a resolution of 1° . At each step, a tilted-ring model of the object is built in 3D-Barolo according to the specified parameters and inclination value; the synthesized moment zero map for this model is then compared to a true moment zero map created directly from the data. Residuals are calculated on a pixel-by-pixel basis as the absolute value of the difference between the model and the true map, then summed over the entire image. The inclination value that produces the smallest summed residual is taken as the output of this step.

However, we note that in order to produce the two-ring base model in the very first step, we must provide 3D-Barolo with an initial inclination value. Therefore this process must be repeated several times, iterating through a fixed set of initial inclination values; for these sources, the set was $\{15^\circ, 30^\circ, 45^\circ, 60^\circ, 75^\circ\}$. Ideally, the result will vary by only a few degrees; then an intermediate inclination value is found by simply taking the average of these results. This value can be checked against itself by repeating the iteration process, this time using the average as the initial inclination. If the output inclination of this step is the same as the initial value to within $\sim 1^\circ$, it is taken as the final value. Otherwise, the iteration process is again repeated, this time using the newest output inclination as the initial value. In both successful models, no further steps were necessary to determine the inclination.

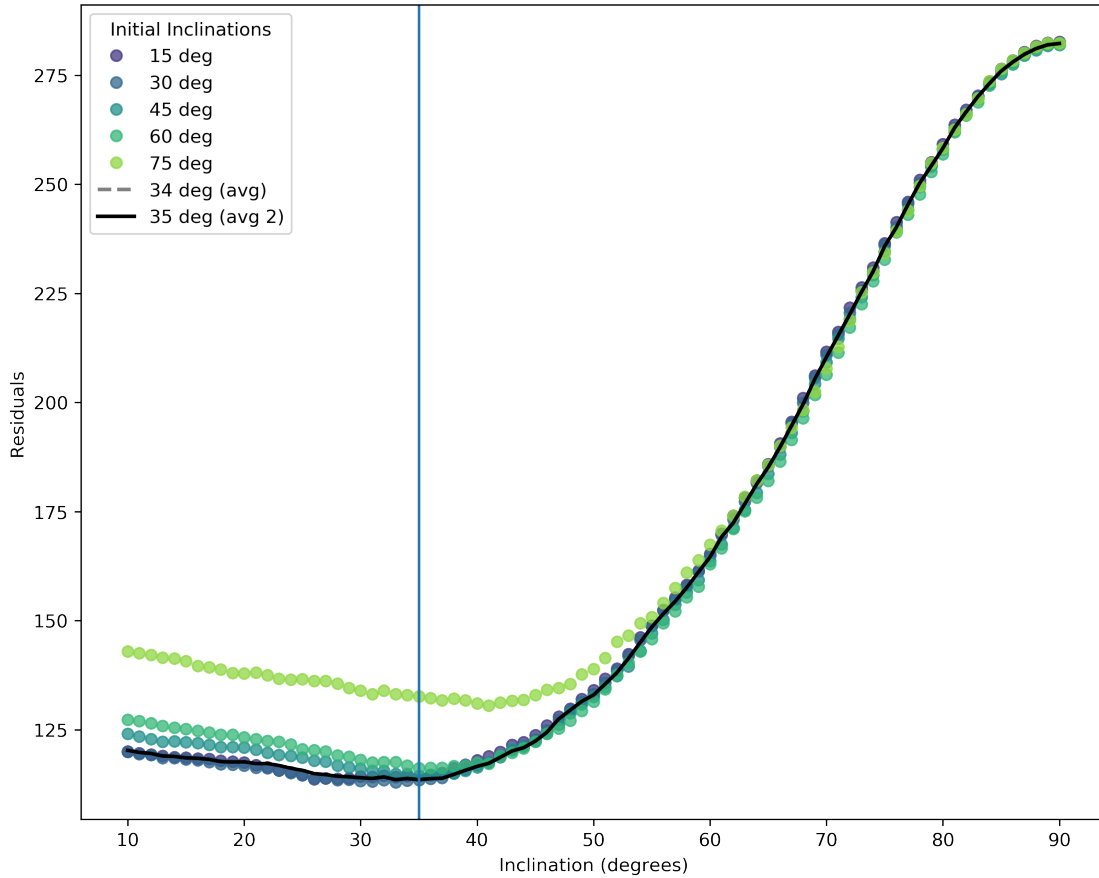


Figure 7: The derivation of the inclination of AGC 198606. Dotted curves show residuals as a function of varying inclination when compared to a true moment zero map. The minima of each of these curves, ranging from 29° to 41° , was averaged to produce the final curves in gray and black. The final value of 35° is highlighted by the vertical line. The nearly-flat shape of the curves to the left of their minima suggest that the inclination may be even lower than 35° .

Once the inclination of a source has been determined using this method, higher-resolution modeling may be attempted. Results of two such efforts are presented in the following sections.

3.2 AGC 198606

Following the procedure outlined in section 3.1, AGC 198606 yields an inclination of 35° ; the results of this process are shown in Figure 7.

We then apply a fixed inclination of 35° and a position angle of 140° to maximize the velocity extent of the position-velocity slice. We allow only the rotational and dispersion

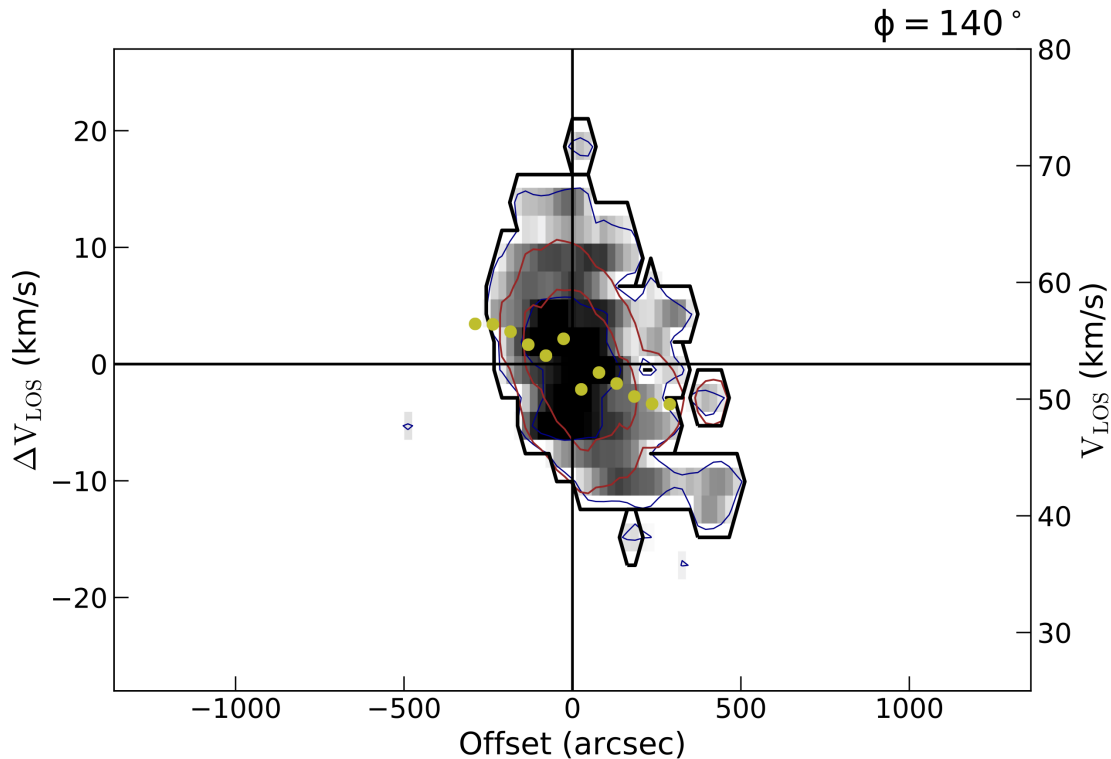


Figure 8: A major-axis position-velocity slice for AGC 198606. The slice is centered near the location of the maximum HI mass surface density and cuts through the source at a position angle meant to maximize the velocity gradient. The thick black contour shows the outline of the mask imposed by 3D-Barolo. Thinner contours for the data (blue) and model (red) appear at levels $2^n \cdot c_{\min}$, where $c_{\min} = 0.0059 \text{ Jy beam}^{-1}$ and $n = 0, 1, \dots, 8$. Green points show the rotational velocity calculated in each ring built by 3D-Barolo; these points form a preliminary rotation curve.

velocities to vary as each ring is built. We sample the map by changing the radius by half a beam width ($52.5''$) on each step; this oversamples the data, so the points are not independent, but we earn more rings to fit to the data. 3D-Barolo converges under these conditions, producing outputs including the position-velocity (PV) slice in Figure 8. The magnitude of the projected velocity gradient in this PV slice is approximately 30 km s^{-1} over $12'$; if interpreted as rotation, this would correspond to a rotation velocity on the order of 15 km s^{-1} . The rotation curve does not attain the flat shape traditionally expected for a dark matter halo, but this is not unusual for dwarf galaxies (Swaters et al., 2009).

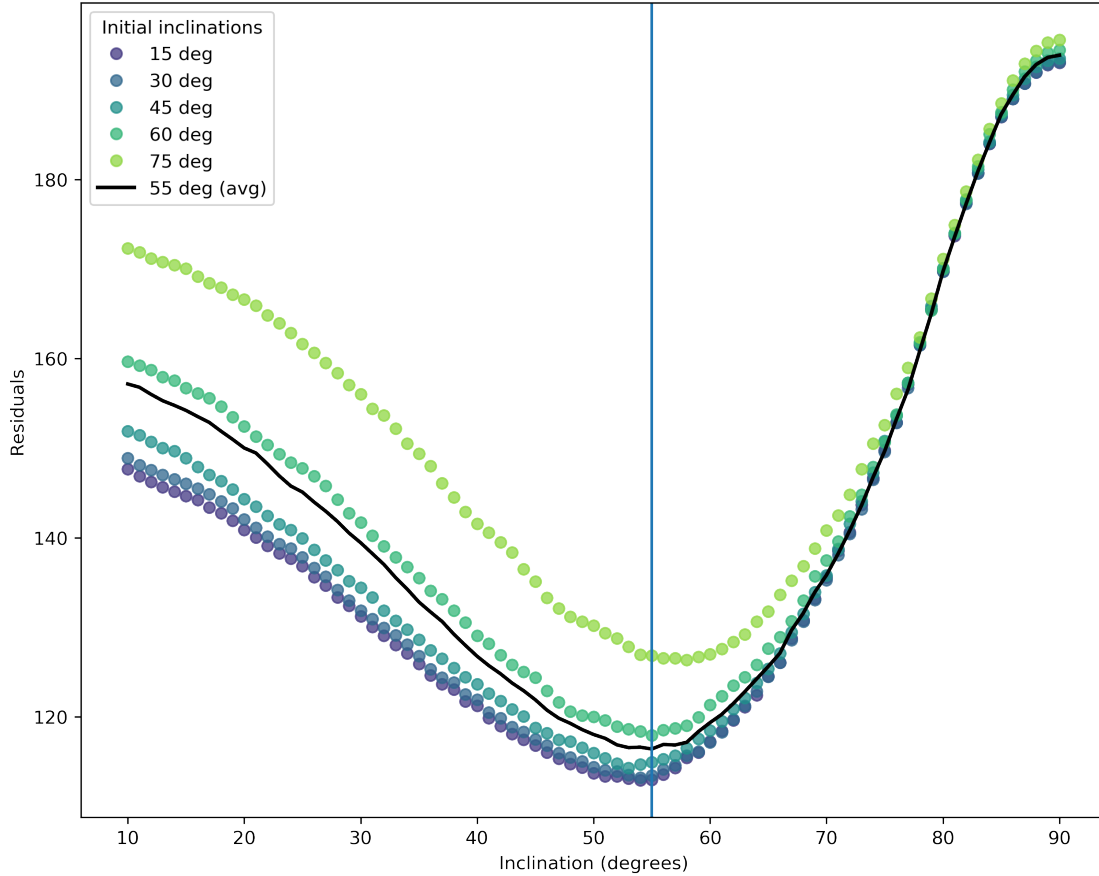


Figure 9: The derivation of the inclination of AGC 249525. Dotted curves show residuals as a function of varying inclination when compared to a true moment zero map. The minima of each of these curves, ranging from 53° to 59° , was averaged to produce the final curves in gray and black. The final value of 55° is highlighted by the vertical line. The near-parabolic shape of the curves, with little flattening around the minimum, suggest a high level of confidence on the final value.

3.3 AGC 249525

Following the procedure outlined in section 3.1, AGC 249525 yields an inclination of 55° ; the results of this process are shown in Figure 9.

We apply an inclination of 55° and a position angle of 165° , again allowing only the rotational and dispersion velocities to vary. We again oversample the map by half a beam width ($52.5''$). 3D-Barolo converges under these conditions, producing outputs including the position-velocity (PV) slice in Figure 10. The magnitude of the projected velocity gradient in this PV slice is approximately 30 km s^{-1} over $10'$; if interpreted as rotation, this would correspond to a rotation velocity on the order of 15 km s^{-1} . The peak in the first point of

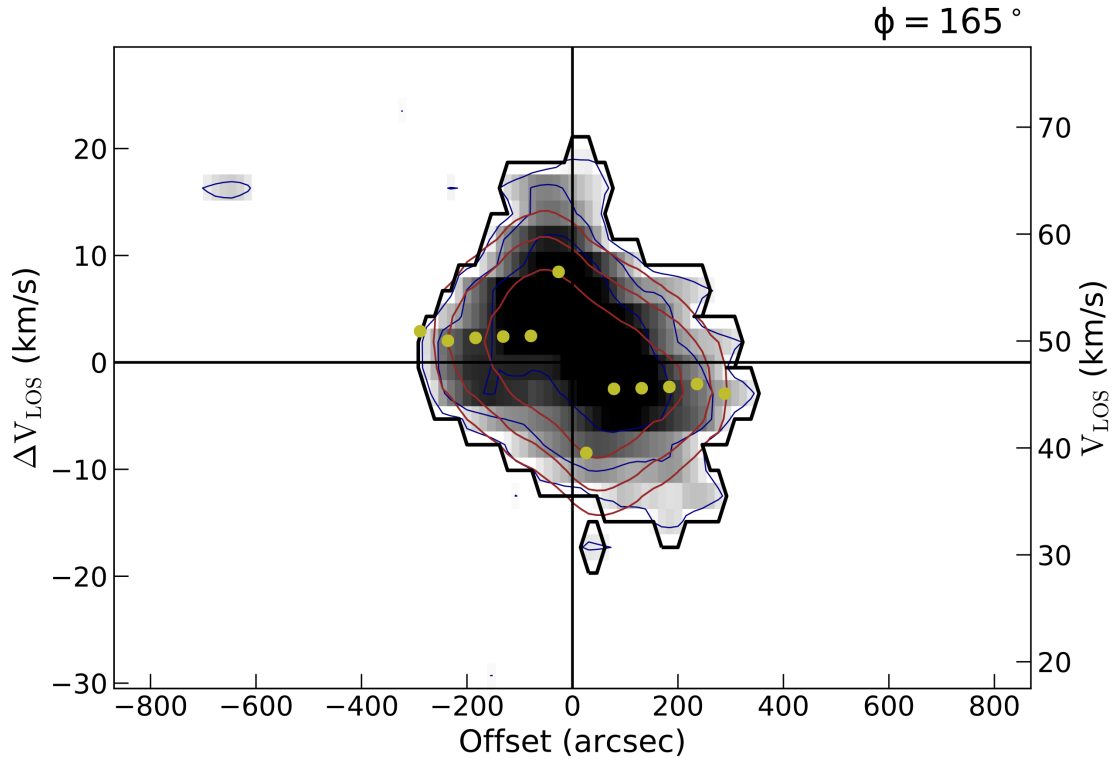


Figure 10: A major-axis position-velocity slice for AGC 249525. The slice is centered near the location of the maximum HI mass surface density and cuts through the source at a position angle meant to maximize the velocity gradient. The thick black contour shows the outline of the mask imposed by 3D-Barolo. Thinner contours for the data (blue) and model (red) appear at levels $2^n \cdot c_{\min}$, where $c_{\min} = 0.0036 \text{ Jy beam}^{-1}$ and $n = 0, 1, \dots, 8$. Green points show the rotational velocity calculated in each ring built by 3D-Barolo; these points form a preliminary rotation curve.

the rotation curve could be a result of oversampling in the model; further optimization of model parameters and higher-resolution images may help to correct this.

3.4 Other sources

Although 3D-Barolo does not require a coherent velocity gradient in order to converge, the majority of its outputs become meaningful only if one is present. Of the six sources presented in this work, AGC 198606 and AGC 249525 were certainly the two most promising in this respect. AGC 258237 and AGC 268069 show potential for structure in their velocity fields, although their HI appears to be separated into multiple clouds; these properties are worthy of further investigation in a future work. AGC 215417 and AGC 219656 show the most limited structure in their velocity fields; although they merit study in other ways, they will

likely continue to be excluded from modeling efforts with 3D-Barolo.

4 Results

4.1 HI morphology

HI imaging of these sources reveals a varied set of HI morphologies, from largely singular contiguous clouds to collections thereof. Two sources (AGC 198606 and AGC 249525) show “galaxy-like” gas morphologies, constraining emission to a single contiguous cloud (although both have “tails” that may yet be artifacts of the imaging process—see Figures 1 and 4). Two more (AGC 215417 and AGC 219656) are similarly constrained to an obvious primary cloud, but may have rotation speeds low enough that we only observe dispersion. A third pair (AGC 258237 and AGC 268069) have unusual gas morphologies, appearing with two or more distinct column density peaks that suggest the separation of the emission into multiple clouds. This property complicates the comparison to ALFALFA data, as more regions of emission may have been included here than in the ALFALFA detections, resulting in higher integrated flux densities than expected.

Regardless, all sources have exceptionally low surface brightnesses, with peak column densities remaining below 10^{20} atoms cm^{-2} (see Table 2). This is at odds to column density values for “typical” dwarf galaxies, which regularly reach orders of 10^{21} atoms cm^{-2} (Teich et al., 2016). Without the presence of dense gas, we may argue that star formation would be suppressed in such sources, which would agree with the very faint stellar overdensities that have so far been captured for these UCHVCs (Janesh et al., 2019).

4.2 HI kinematics

Two of the sources (AGC 198606 and AGC 249525) show velocity gradients indicative of rotation support that visible in the calibrated images and corroborated by 3D-Barolo models. Two more (AGC 258237 and AGC 268069) have unusual HI morphologies as discussed in

section 4.1. This complicates the modeling process, as it is difficult for 3D-Barolo to build a tilted-ring model across multiple clouds. However, these sources have structure in their most prominent clouds that could suggest a velocity gradient, and are therefore worthy of further investigation. The remaining two sources (AGC 215417 and AGC 219656) have gas kinematics that are unusual compared to those found in gas-rich dwarf galaxies; they appear to be dispersion- rather than rotation-dominated, as evidenced by the inefficacy of 3D-Barolo models in deciphering their structure.

The two sources with promising velocity gradients are the most likely to host ordered motion; two more are again worthy of further investigation. As work continues on the derivation of rotation curves for these sources, we will be able to investigate the possibility of these sources being hosted by dark matter halos. Being such low-mass sources at the tail end of the HI mass function, these sources could provide interesting insight and connections to dark matter halo and scaling relations (Salucci & Burkert, 2000; Salucci et al., 2012; Lapi et al., 2018).

5 Summary and future work

In this work, we present VLA HI observations of six UCHVCs originally identified in the ALFALFA survey as promising galaxy candidates and later found by Janesh et al. (2019) to have possible stellar counterparts. We employ multiple imaging methods and compare their results, both to each other and to the previously measured ALFALFA values. We then fit 3D tilted-ring models to our images generated by 3D-Barolo. From our images and 3D-Barolo models, we are able to discern the best galaxy candidates and provide initial estimates of several of their properties. However, more work is necessary to produce the best possible results:

- The integrated HI flux densities yield consistently lower values than those found by ALFALFA. A reinvestigation of the imaging process is required to ensure that all flux is being recovered. One potential step may involve additional smoothing of the data during creation of the moment maps.

- Once the imaging process has been changed to yield satisfactory flux recovery, the most promising galaxy candidates may be re-imaged at higher angular resolution for a deeper exploration of their morphology and kinematics.
- The full capabilities of 3D-Barolo have not yet been explored in this work. The model parameters may be further optimized in order to produce the best possible rotation curves. Higher-resolution imaging of the best galaxy candidates will also allow for proportionally higher-resolution modeling.
- Reliable derivation of rotation curves will make possible the calculation of the dynamical masses of the most promising candidates. The differences between the dynamical masses and the projected HI and stellar masses provide insight on the dark matter halos expected to host these sources.

Acknowledgments

I am deeply grateful for Dr. Betsey Adams, who not only gave me the chance to come work with her in the Netherlands for a summer, but has continued to offer her guidance and support throughout this work. I'm incredibly lucky to be able to call her a colleague. Special thanks must also go to Prof. John Cannon, who has served as my advisor at Macalester for the past four years. I am a better scientist and a better person for having been his student.

Pavel Mancera Piña was instrumental for his knowledge of 3D-Barolo and willingness to share his expertise with a stubborn undergraduate, even after I returned to Macalester (a full seven time zones away). I would also have been lost without Susie Paine, CASA tamer and copy editor extraordinaire. She and the other regular inhabitants of Olin-Rice kept me sane throughout this process; they witnessed my moments of crisis, celebrated my small victories, and provided caffeine at crucial times. May shouts of "SET!" ring out through the physics wing for years to come.

I thank the anonymous referees for their insightful comments. This research was funded in part by ASTRON and their outstanding summer student programme, and supported by Macalester College through an Independent Study course.

References

- Adams, E. A. K., Giovanelli, R., & Haynes, M. P. 2013, *ApJ*, 768, 77
- Adams, E. A. K., & Oosterloo, T. A. 2018, *A&A*, 612, A26
- Adams, E. A. K., Oosterloo, T. A., Cannon, J. M., Giovanelli, R., & Haynes, M. P. 2016, *A&A*, 596, A117
- Bullock, J. S., & Boylan-Kolchin, M. 2017, *ARA&A*, 55, 343
- Di Teodoro, E. M., & Fraternali, F. 2015, *MNRAS*, 451, 3021
- Giovanelli, R., Haynes, M. P., Kent, B. R., & Adams, E. A. K. 2010, *ApJ*, 708, L22
- Janesh, W., Rhode, K. L., Salzer, J. J., et al. 2017, *ApJ*, 837, L16
- . 2019, *AJ*, 157, 183
- . 2015, *ApJ*, 811, 35
- Klypin, A., Kravtsov, A. V., Valenzuela, O., & Prada, F. 1999, *ApJ*, 522, 82
- Lapi, A., Salucci, P., & Danese, L. 2018, *ApJ*, 859, 2
- McMullin, J. P., Waters, B., Schiebel, D., Young, W., & Golap, K. 2007, *Astronomical Society of the Pacific Conference Series*, Vol. 376, *CASA Architecture and Applications*, 127
- McQuinn, K. B. W., Skillman, E. D., Dolphin, A., et al. 2015, *ApJ*, 812, 158
- Peebles, P. J. E. 2001, *ApJ*, 557, 495
- Salucci, P., & Burkert, A. 2000, *ApJ*, 537, L9
- Salucci, P., Wilkinson, M. I., Walker, M. G., et al. 2012, *MNRAS*, 420, 2034
- Swaters, R. A., Sancisi, R., van Albada, T. S., & van der Hulst, J. M. 2009, *A&A*, 493, 871
- Teich, Y. G., McNichols, A. T., Nims, E., et al. 2016, *ApJ*, 832, 85